

- [21] J. Talairach and P. Tournoux, *Co-Planar Stereotaxic Atlas of the Human Brain*. New York: Thieme Medical, 1988.
- [22] D. N. Kennedy, P. A. Filipek, and V. S. Caviness, Jr., "Anatomic segmentation and volumetric calculations in nuclear magnetic resonance imaging," *IEEE Trans. Med. Imag.*, vol. 8, pp. 1–7, Feb. 1989.
- [23] J. C. Russ, *The Image Processing Handbook*, 2nd ed. Boca Raton, FL: CRC, Inc., 1995.
- [24] D. Gutfinger, E. Hertzberg, T. Tolxdorff, F. Greensite, and J. Sklansky, "Tissue identification in MR images by adaptive cluster analysis," in *Proc. Medical Imaging V: Image Processing*, San Jose, CA, Feb. 27–Mar. 1, 1991, vol. 1445, pp. 288–296.

An Improved Algorithm for Rotational Motion Artifact Suppression in MRI

Chaminda Weerasinghe* and Hong Yan

Abstract—An improved algorithm for planar rotational motion artifact suppression in standard two-dimensional Fourier transform magnetic resonance images is presented. It is shown that interpolation of acquired view data on the uncorrupted k -space create data overlap and void regions. We present a method of managing overlap data regions, using weighted averaging of redundant data. The weights are assigned according to a priority ranking based on the minimum distance between the data set and the k -space grid points. An iterative estimation technique for filling the data void regions, using projections onto convex sets (POCS), is also described. The method has been successfully tested using computer simulations.

Index Terms—Image reconstruction, MRI, POCS, rotational motion artifacts.

I. INTRODUCTION

Rotational motion artifacts are notably prevalent in magnetic resonance images (MRI's) such as of head, brain, and limbs. Even a slight rotation during the data acquisition can cause significant artifacts in the reconstructed image, which obscure vital anatomical detail. Several publications have proposed methods of reducing such artifacts [1]–[5]. However, most of these methods are limited to suppression of small angle rotational artifacts. In this paper, an improved method, capable of suppressing rotational motion artifacts due to large angle rotations of the imaged object, is presented. Only gross rotations in the imaging plane are considered. The movement is assumed to be sufficiently slow, that the imaged object is considered to be stationary during the acquisition of a single view of data. Hence, the motion is an interview effect, a condition which is generally satisfied in the case of gross movement [6]. The rotation angles at the acquisition of each view are considered known, using sensors or postprocessing techniques [1], [2], [4].

It has been shown that, in-plane rigid rotations around arbitrary points in the field of view (FOV) can be modeled by separate

Manuscript received July 14, 1997; revised February 19, 1998. The Associate Editor responsible for coordinating the review of this paper and recommending its publication was M. W. Vannier. Asterisk indicates corresponding author.

*C. Weerasinghe is with the Electrical Engineering Department, University of Sydney, Sydney, NSW 2006 Australia (e-mail: chaminda@ee.usyd.edu.au).

H. Yan is with the Electrical Engineering Department, University of Sydney, Sydney, NSW 2006 Australia.

Publisher Item Identifier S 0278-0062(98)04882-4.

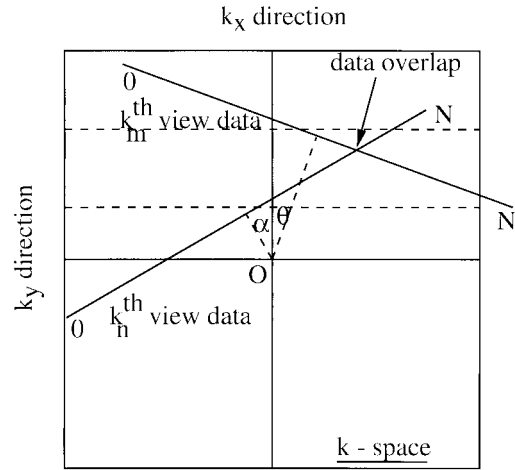


Fig. 1. Illustration of data overlap between two views, on the k -space of the imaged object.

two-dimensional (2-D) translations and rotations around the origin [1]. Since the correction techniques for translational motion artifacts are well established via scores of publications, this paper will only delve into the effects of the rotational component around the origin. Such a rotation tends to rotate the locations of the spatial frequency components around the origin of the k -space [1]. A popular correction method is to use bilinear interpolation in the spatial domain followed by super-position on to the corrected k -space [1]. However, this method is shown to create regions of data overlap and data void regions, causing degradation of the final image quality, which become pronounced when the rotation angles are large.

II. DATA OVERLAP AND VOID REGIONS

If the imaged object is rotated at an angle θ , at the acquisition of the k_m th view, the relationship between the acquired corrupted signal S' and the required k -space data S can be given by

$$S'(k_x, k_m) = S(\bar{k}_x, \bar{k}_y) \quad (1)$$

where $\bar{k}_x = k_x \cos \theta + k_m \sin \theta$ and $\bar{k}_y = -k_x \sin \theta + k_m \cos \theta$.

Since the motion is considered to be an interview effect, θ is constant during the acquisition of all N samples in the frequency encoded k_x direction.

If the k_m th view is rotated by an angle θ and the k_n th view is rotated by a different angle α , the acquired data samples denoted by $S'(k_{xm}, k_m)$ and $S'(k_{xn}, k_n)$ both represent the same spatial frequency information in the uncorrupted k -space, provided that the following conditions are satisfied:

$$\begin{aligned} k_{xm} \cos \theta + k_m \sin \theta &= k_{xn} \cos \alpha + k_n \sin \alpha \\ -k_{xm} \sin \theta + k_m \cos \theta &= -k_{xn} \sin \alpha + k_n \cos \alpha \end{aligned} \quad (2)$$

where $k_m \neq k_n$, $\theta \neq \alpha$ and $0 \leq k_{xm}, k_{xn} \leq N$.

Therefore, when projected on to the uncorrupted k -space, data overlap will occur between the k_{xm} th sample of the k th view and the k_{xn} th sample of the k_n th view, as shown in Fig. 1.

Data overlapping can occur between any number of different views, rotated at different angles, hence, producing significant regions of data overlap. Only $N \times N$ data samples are acquired from all the N views, and there are $N \times N$ grid points required to be filled in

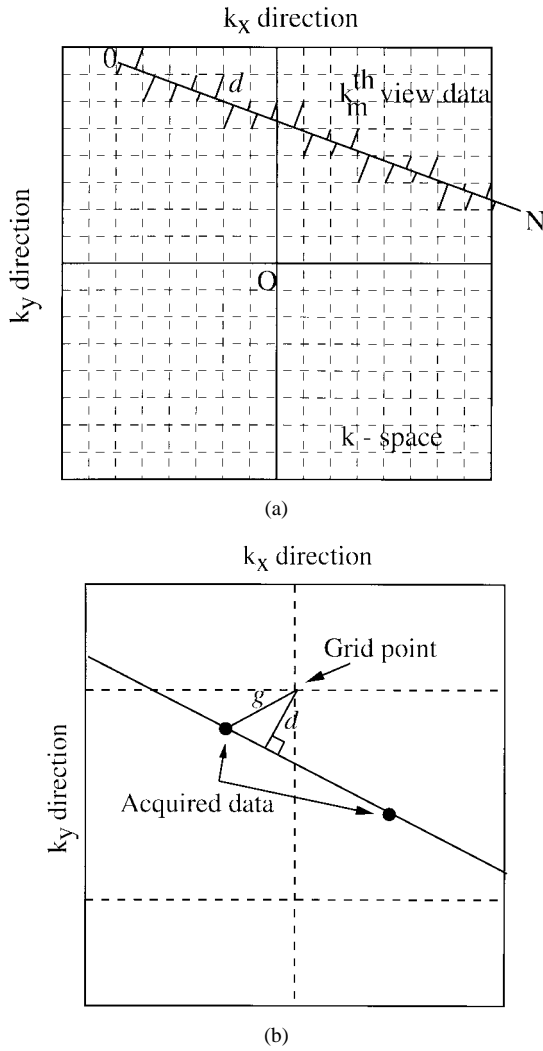


Fig. 2. (a) Deviation between the acquired view data and the required grid points. (b) Graphical representation of the distance “ d ”.

the uncorrupted k -space. Therefore, if some of the grid points are over represented due to data overlap, it is logical to expect some grid points to be under represented due to data voids.

III. MANAGEMENT OF OVERLAP DATA

At a data overlap, the interpolation errors associated with each data sample can differ considerably. Therefore, in practice, we can rank the overlapping samples at a particular grid point, according to their interpolation accuracy. Such a system of ranking enables us to attach weights to each sample, prior to computing the average spatial frequency value at a particular grid point in the corrected k -space. Weighted averaging of redundant data can lead to improved performance under noisy conditions.

In bilinear superposition algorithm [1], the interpolation was performed in the spatial domain, which reduced the interpolation errors caused by high variance in the spatial frequency data. However, we cannot discount the fact that each of the interpolations is performed using only a single view of data at a time. Effectively, the attempt is to interpolate values on to a 2-D grid using one-dimensional signal data spanning on an inclined line on the 2-D k -space. The adjacent grid points to this inclined line are filled using interpolated values as shown in Fig. 2(a). Obviously, the more the deviation (d) of the

grid point from the inclined line, the less accurate the interpolated value be.

Notice that “ d ” is not the offset distance between the nearest data sample and the grid point which is represented by “ g ” in Fig. 2(b). Since acquired data are available along the inclined line, the interpolation error associated with this direction is significantly lower compared to the interpolation error associated with the direction perpendicular to the inclined line, along which there are no data available. Therefore, the ranking is based on the distance “ d ” between the prospective grid point and the nearest view, which is given by

$$d = |k_{yo} \cos \theta + k_{xo} \sin \theta - k_m| \quad (3)$$

where (k_{xo}, k_{yo}) are the coordinates of the grid point, θ is the rotation angle, and k_m is the phase-encoded view number.

Therefore, the weight w_r related to the r th sample S_r in an overlap region can be assigned as follows:

$$w_r = \frac{1}{d_r}. \quad (4)$$

The corrected spatial frequency value $S(k_x, k_y)$ at (k_x, k_y) grid point in the k -space can be computed using

$$S(k_x, k_y) = \frac{\sum_{r=1}^m w_r S_r}{\sum_{r=1}^m w_r} \quad (5)$$

where m is the total number of competing samples.

The algorithm to manage data overlap can be formulated as follows.

- 1) Divide the acquired views in to p different groups, each containing a set of views subjected to rotations at same angle. Grouping such views together not only reduces interpolation errors but also decreases the reconstruction time. If there are p such groups (i.e., $p \leq N$), only p transformations to the spatial domain are required, instead of N , to perform interpolations. If the motion is continuous, then $p = N$.
- 2) Insert each group in to a zeroed $N \times N$ complex matrix.
- 3) Calculate the inverse 2-D Fourier transform (FT) of the p different matrices.
- 4) Using bilinear interpolation, back-rotate each of the p different images by the known rotation angle.
- 5) Calculate the 2-D FT of the p different images.
- 6) Compute the “ d ” values corresponding to each sample.
- 7) If a particular grid point does not have a view within “ d ” value of unity, such a grid point is masked and set to zero. This step is included to eliminate any leakage spatial frequency components generated due to interpolation in the spatial domain. The resulting spatial frequency values are at most one unit away from the acquired view which spans on an inclined line.
- 8) Calculate the weights associated with each corrected k -space value.
- 9) Compute the weighted average values at each k -space grid point.

IV. ITERATIVE ESTIMATION OF MISSING DATA

Although reconstructed image quality can be partly enhanced by weighted averaging of redundant data, the data void regions in the corrected k -space may still degrade the final image quality, by the way of reduced intensity at particular regions and blurred edges caused by the nonavailability of particular spatial frequency components.

An analytical method using least squares error (LSE) technique to estimate low spatial frequency values was proposed by Yan *et al.* [7]. This method is limited to estimating very small number of missing data, where the number of unknowns is much smaller than the number of equations in the LSE problem. However, when the number of required estimations increases, the problem becomes ill posed and the estimation is observed to be noise sensitive and computationally unstable.

Since the rotations at large angles produce large data void regions, the estimation technique is required to be capable of estimating in excess of 10000 samples for a 256×256 image. Therefore, the analytical method [7] is ineffective due to the ill posedness and prohibitive computational complexity.

The problem of estimating missing spatial frequency values is frequently encountered in computed tomography (CT) [8]–[11] and in confocal scanning microscopy [12]. This problem is named the “missing cone problem” and several methods have been proposed in literature, to suppress the artifacts in the reconstructed image. However, there are some problem specific information regarding the missing cone problem, which are not valid for the frequency estimation problem described in this paper. The noniterative solutions to the missing cone problem, that range from 2-D extrapolation in the Fourier domain [8] to multicose sampling approach [9], all use the problem specific information such as 1) missing spatial frequencies are restricted to a cone shaped region and 2) the complete sinograms of acquired data possess bowtie-shaped spectral support. The proposed iterative techniques mostly use projections on to convex sets (POCS) as the basis of the algorithm [11]. A technique using artificial neural network (ANN) has been proposed [10]. However, the neural network structure is dependent upon the problem specific information, which inhibits its application to a general problem such as the one introduced in this paper.

Considering the arbitrary shape of the data missing regions and the available *a priori* information on the imaged object, the method of POCS was found to be an effective and efficient technique to estimate a large number of missing spatial frequency values.

POCS is an iterative algorithm for finding a solution g that satisfies constraints corresponding to convex sets in a Hilbert space \mathcal{H} [13]. Each element in \mathcal{H} is considered to be an image. Each *a priori* information or constraint restricts the solution to a closed convex set in \mathcal{H} . A subset \mathcal{C} of a Hilbert space \mathcal{H} is said to be convex if together with any a and b it also contains $\mu a + (1 - \mu)b$ for all $\mu, 0 \leq \mu \leq 1$ [13].

If there are m closed convex sets $\mathcal{C}_i \in \mathcal{H}$, corresponding to m number of *a priori* information, then

$$g \in \mathcal{C}_o = \bigcap_{i=1}^m \mathcal{C}_i \quad (6)$$

provided that the intersection \mathcal{C}_o is nonempty. Given the constraint sets \mathcal{C}_i and their respective projection operators P_i , the iterative sequence is given by

$$g_{k+1} = \left(\prod_{i=1}^m P_i \right) g_k. \quad (7)$$

The above sequence converges weakly to a feasible solution in the intersection \mathcal{C}_o of the constraint sets [14]. The more general form of the (7) is

$$g_{k+1} = \left(\prod_{i=1}^m T_i \right) g_k \quad (8)$$

where $T_i = (1 - \lambda_i)I + \lambda_i P_i, 0 < \lambda_i < 2$. λ_i is the relaxation parameter, and can be used to accelerate the rate of convergence of

the algorithm. However, a single set of λ_i 's may not be effective at all signal-to-noise ratios (SNR's) [11].

It should be noted that any solution in the set \mathcal{C}_o is consistent with the given constraints and therefore a feasible solution. In general, there are infinitely many feasible solutions. It can also be shown that different initial estimates may lead to different solutions.

The following sets and their corresponding projection operators are used to estimate the missing spatial frequency components:

1) *Finite Support Constraint*: The image has a finite region of interest (ROI) bounded by the outer boundary of the imaged object. Therefore, ROI is everything but the background of the image. Each iteration of the algorithm should minimize the pixel energy outside the ROI

$$\mathcal{C}_1 = \{g(x, y): g(x, y) = 0, \quad \text{for } (x, y) \notin \text{ROI}\} \quad (9)$$

where the projection operator is given by

$$P_1 g = \begin{cases} g, & \text{if } (x, y) \in \text{ROI} \\ 0, & \text{otherwise.} \end{cases} \quad (10)$$

2) *Consistency Constraint*: A specified region in the k -space contains spatial frequency data interpolated from the available acquired data. Therefore, error between the interpolated values and the k -space values of the image reconstructed at the each iteration, should be minimized

$$\mathcal{C}_2 = \{g(x, y): G(k_x, k_y) = S(k_x, k_y) \forall (k_x, k_y) \in R_o\}. \quad (11)$$

$G(k_x, k_y)$ is the FT of $g(x, y)$, $S(k_x, k_y)$ is the k -space obtained by the application of the algorithm in Section III, and R_o represent all the nonzero k -space grid points in $S(k_x, k_y)$. The projection operator is given by

$$P_2 g = \mathcal{F}^{-1} \begin{cases} S(k_x, k_y), & \text{if } (k_x, k_y) \in R_o \\ G(k_x, k_y), & \text{otherwise.} \end{cases} \quad (12)$$

3) *Maximum Pixel Sum and Positivity Constraint*: The total pixel sum of the reconstructed image should be equal to a known value A , where $A \approx S'(0, 0)$. It is also known that all the pixel values should be positive and real values

$$\mathcal{C}_3 = \left\{ g(x, y): g(x, y) = \frac{A}{\epsilon} g(x, y) \text{ if } \text{Re}(g) > 0 \right\} \quad (13)$$

where $\text{Re}(g)$ is the real part of $g(x, y)$ and

$$\epsilon = \sum_{x=0}^{N-1} \sum_{y=0}^{N-1} g(x, y).$$

The projection operator is given by

$$P_3 g = \begin{cases} 0, & \text{if } \text{Re}(g) \leq 0 \\ \frac{A}{\epsilon} \text{Re}(g), & \text{if } \text{Re}(g) > 0. \end{cases} \quad (14)$$

4) *Amplitude Constraint*: The amplitudes of all $g(x, y)$ must lie within a prescribed closed interval $[0, 255]$

$$\mathcal{C}_4 = \{g(x, y): 0 \leq g(x, y) \leq 255\}. \quad (15)$$

The projection operator is given by

$$P_4 g = \begin{cases} 0, & \text{if } g(x, y) < 0 \\ 255, & \text{if } g(x, y) > 255 \\ g(x, y), & \text{if } 0 \leq g(x, y) \leq 255. \end{cases} \quad (16)$$

Since POCS method does not converge to a unique solution, the resulting reconstructed image may diverge from the desired solution while converging simultaneously to all the given constraints. Therefore, a regulatory indicator of closeness to the solution is required. The known information on the rotational motion parameters

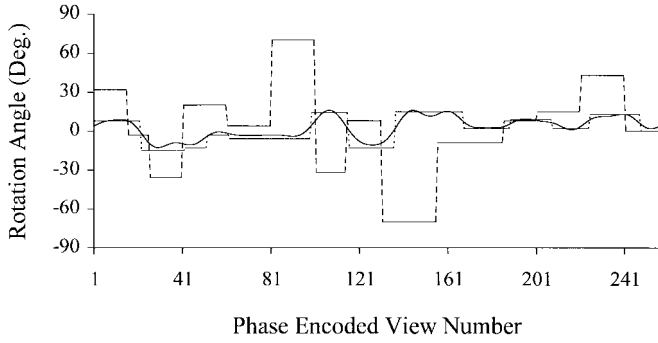


Fig. 3. Rotational motion parameters for each phase encode. Case 1: - - -, Case 2: - . - , Case 3: —.

can be used for this purpose. It is possible to estimate the artifactual image from the solution at the i th iteration $g_i(x, y)$, using (17)

$$\hat{m}(x, y) = \mathcal{F}^{-1} \left[\sum_{x=0}^{N-1} \sum_{y=0}^{N-1} g_i(\bar{x}, \bar{y}) e^{-i(2\pi/N)(xk_x + yk_y)} \right] \quad (17)$$

where $\bar{x} = x \cos \theta(k_y) - y \sin \theta(k_y)$ and $\bar{y} = x \sin \theta(k_y) + y \cos \theta(k_y)$ is the angle of rotation at the k_y th phase encode. \mathcal{F}^{-1} represents the inverse FT. The estimated artifactual image is $\hat{m}(x, y)$.

The artifactual image $m'(x, y)$ can be directly computed using inverse FT on the acquired data. The regulatory error metric can then be defined based on the difference between the estimated and computed artifactual images, as given in (18). More specifically, we are seeking $g_i(x, y)$ that minimizes the difference between $\hat{m}(x, y)$ and $m'(x, y)$

$$E = \frac{\sum_{x=0}^{N-1} \sum_{y=0}^{N-1} \|\hat{m}(x, y) - m'(x, y)\|}{\sum_{x=0}^{N-1} \sum_{y=0}^{N-1} \|m'(x, y)\|} \times 100\%. \quad (18)$$

V. SIMULATION RESULTS AND DISCUSSION

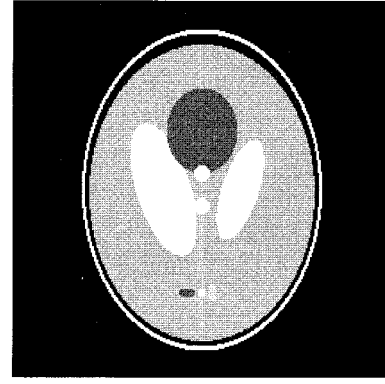
Several simulation experiments were conducted in order to test the effectiveness of the proposed assignment of weights. The Shepp and Logan phantom [15] was used due to the ease of comparison with the bilinear superposition algorithm [1].

The rotational motion artifact was simulated by rotating the phantom by an angle θ prior to obtaining the spatial frequency information for each view. The corrupted N samples of data for the k_y^{th} view is given by

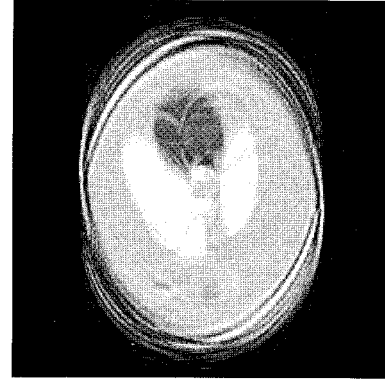
$$S'(k_x, k_y) = \sum_{x=0}^{N-1} \sum_{y=0}^{N-1} m(\bar{x}, \bar{y}) e^{-i(2\pi/N)(xk_x + yk_y)} \quad (19)$$

where $\bar{x} = x \cos \theta - y \sin \theta$ and $\bar{y} = x \sin \theta + y \cos \theta$. k_x is the sample number in the frequency encoded direction, $m(x, y)$ is the original Shepp and Logan phantom, and θ is the angle of rotation for the k_y th view.

Fig. 3 shows the view numbers and corresponding angles of rotation for three different cases studied. The rotations involved stepping as well as continuous motion. The maximum angular span was $\pm 15^\circ$ for Case 1 and Case 3, and $\pm 70^\circ$ for Case 2. The artifactual image for Case 1 is shown in Fig. 4(b).



(a)



(b)

Fig. 4. (a) Shepp and Logan phantom. (b) Computed artifactual image (MSE = 1942.531).

A relative measure on the quality of the reconstructed image was obtained using the mean squared error (MSE), which is defined by

$$\text{MSE} = \frac{1}{N^2} \sum_{x=0}^{N-1} \sum_{y=0}^{N-1} [g(x, y) - m(x, y)]^2 \quad (20)$$

where $g(x, y)$ is the reconstructed image and $m(x, y)$ represent the original image.

The following weighted averaging methods were examined, using three different sets of simulated MR data (i.e., Cases 1–3).

Type 1—Amplitude-Based Weighted Averaging: The higher the amplitude of the overlapping sample, the larger the assigned weight. Therefore, the weight w_r related to the r th sample S_r is given by

$$w_r = |S_r|. \quad (21)$$

Type 2—Rotation Angle-Based Weighted Averaging: The smaller the associated rotation angle of the overlapping sample, the larger the assigned weight. If the rotation angle associated with the r th sample is θ_r , the weight is given by

$$w_r = \frac{1}{\theta_r}. \quad (22)$$

Type 3—Grid Offset-Based Weighted Averaging: The smaller the grid offset “ g ” of the overlapping sample, the larger the assigned weight. The grid offset distance is given by

$$g_r = \sqrt{(\bar{k}_{y_o} - k_y)^2 + (\bar{k}_{x_o} - k_x)^2} \quad (23)$$

where $\bar{k}_{y_o} = k_{y_o} \cos \theta + k_{x_o} \sin \theta$ and $\bar{k}_{x_o} = k_{x_o} \cos \theta - k_{y_o} \sin \theta$. (k_{x_o}, k_{y_o}) are the coordinates of the grid point, k_y is the phase-encoded view number, and k_x is the sample number. Therefore, the

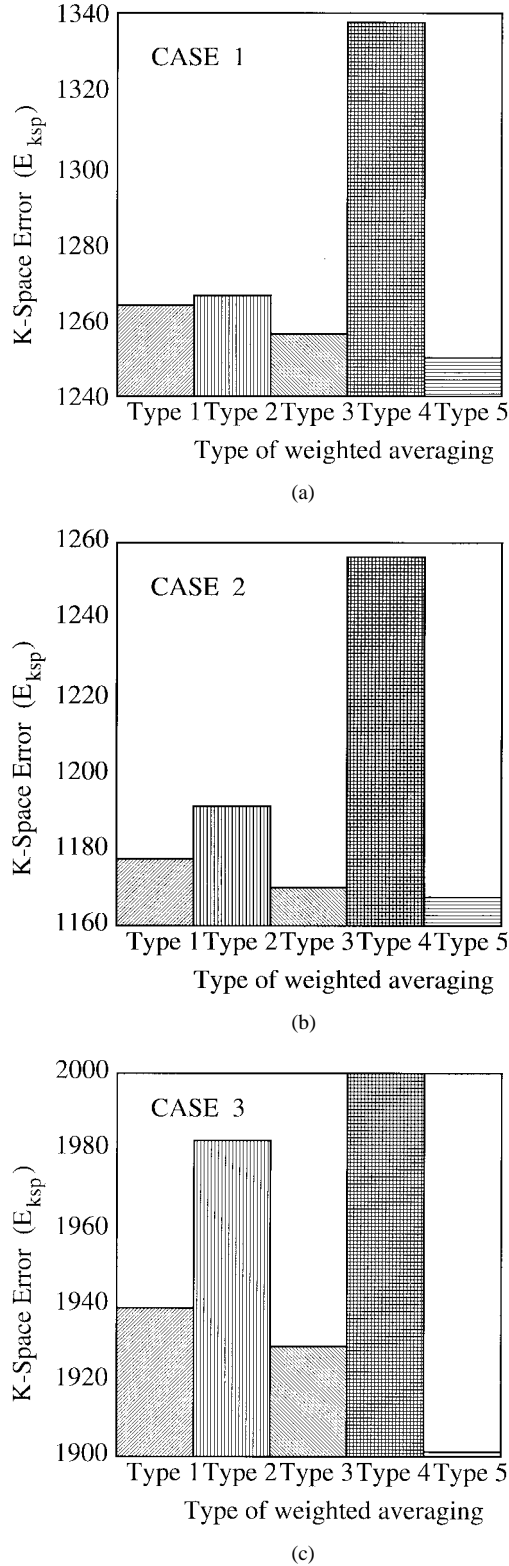
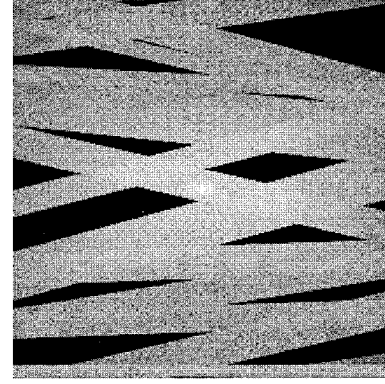


Fig. 5. K -Space error for weighted averaging schemes used: (a) Case 1, (b) Case 2, and (c) Case 3.

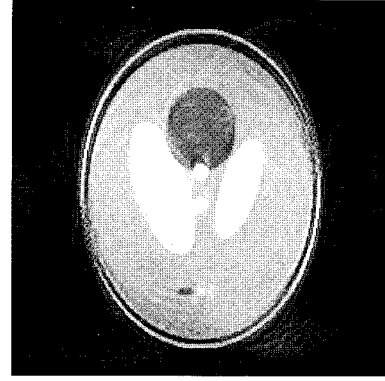
weight is given by

$$w_r = \frac{1}{g_r}. \quad (24)$$

Type 4—Equal Weight Averaging: All the competing samples are assigned the same weight, where the associated weight for any sample



(a)



(b)

Fig. 6. (a) Corrected k -space using BSA. Log magnitude of the spatial frequency components normalized to 0–255. (b) Reconstructed image using BSA (MSE = 541.434).

is given by

$$w_r = 1. \quad (25)$$

Type 5—Proposed Weighted Averaging Scheme: Based on the value of “ d ,” the weight assignment is as given by (4).

The following error metric was used for comparing the accuracy of the corrected k -spaces using different weighted averaging methods:

$$E_{ksp} = \frac{1}{M} \sum_{k_x} \sum_{k_y} |S_r^R(k_x, k_y) - S_r^{(O)}(k_x, k_y)| + \frac{1}{M} \sum_{k_x} \sum_{k_y} |S_i^R(k_x, k_y) - S_i^{(O)}(k_x, k_y)|, \quad \text{for } (k_x, k_y) \in R_{ov} \quad (26)$$

where R_{ov} is the set of all overlapping grid points, and M is the total number of elements in R_{ov} . S^R is the corrected k -space, whereas S^O is the uncorrupted original k -space. S_r and S_i represent the real and imaginary parts, respectively. Fig. 5 presents the performance of weight assignment methods examined. It is clear that the proposed scheme produces the least k -space error.

For Case 1, the bilinear superposition algorithm (BSA) [1] was used first to reconstruct the image for comparison purposes. The resulting corrected k -space and the resultant image are shown in Fig. 6(a) and (b), respectively. The data overlap and void regions can be clearly seen in Fig. 6(a). The improved iterative algorithm was then used to reconstruct the image from the corrupted data. The result after ten iterations is shown in Fig. 7(b) and the corresponding corrected k -space is shown in Fig. 7(a). No regions of data overlap or void are visible in Fig. 7(a).

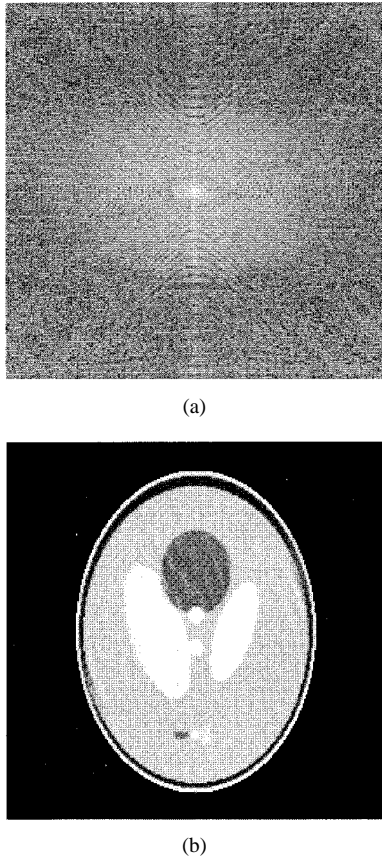


Fig. 7. (a) Corrected k -space using the proposed iterative algorithm. Log magnitude of the spatial frequency components normalized to 0–255. (b) Reconstructed image after ten iterations (MSE = 111.595).

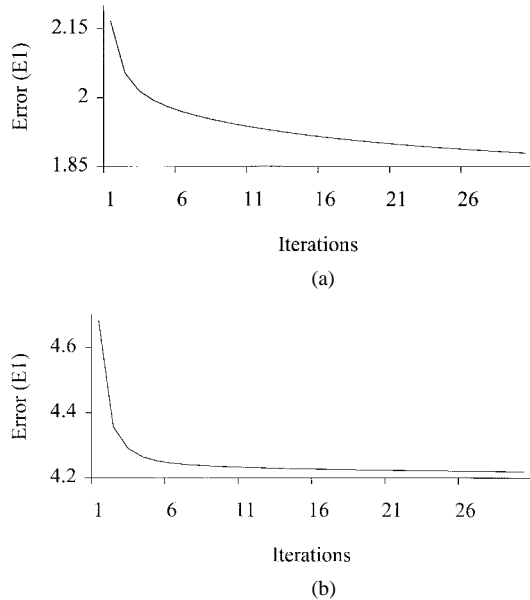


Fig. 8. Variation of the error outside the ROI (E_1) for 30 iterations: (a) Case 1 and (b) Case 2.

To illustrate the convergence of the algorithm, the residual error outside the ROI after each iteration, was used as the error metric, which is given by

$$E_1 = \frac{1}{N^2} \sum_{x=0}^N \sum_{y=0}^N |g_i(x, y)|^2, \quad \text{for } (x, y) \notin \text{ROI} \quad (27)$$

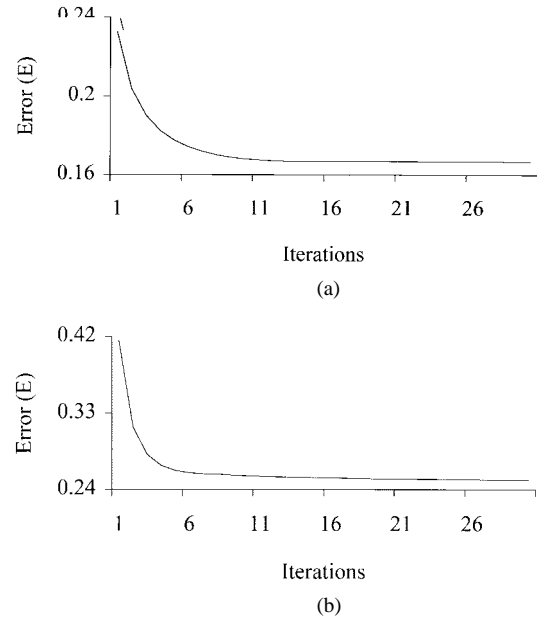


Fig. 9. Variation of the regulatory error metric (E) for 30 iterations: (a) Case 1 and (b) Case 2.

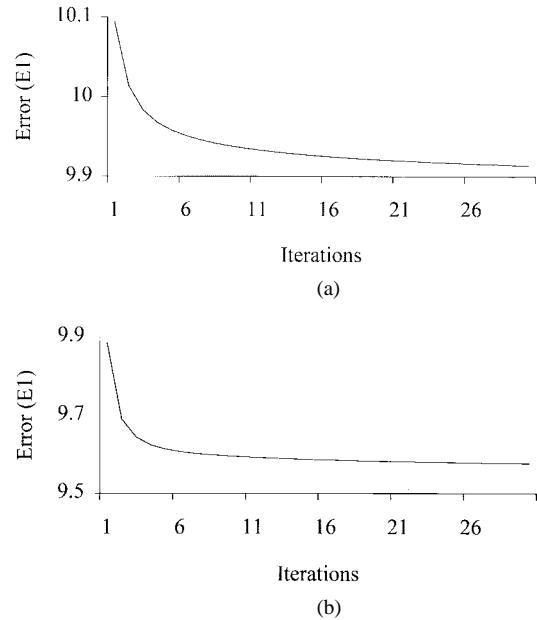


Fig. 10. Variation of the error outside the ROI (E_1) for noisy data (SNR = 10 dB): (a) Case 1 and (b) Case 2.

where $g_i(x, y)$ is the reconstructed image, before the application of the projection operator corresponding to the convex set C_1 , at the i th iteration. If the algorithm is converging, this error should be reduced after each iteration, indicating convergence to the given convex set, as observed in Fig. 8.

Fig. 9 shows the variation of regulatory error metric (E) as given in (18). It should be noted that any solution in the intersection set C_o is consistent with the given constraints and, therefore, a feasible solution.

In general, there are many feasible solutions, if the set C_o contains more than a single element. Therefore, the solution may diverge from the expected result while converging to the intersection set C_o since the algorithm may be converging to another possible solution in C_o .

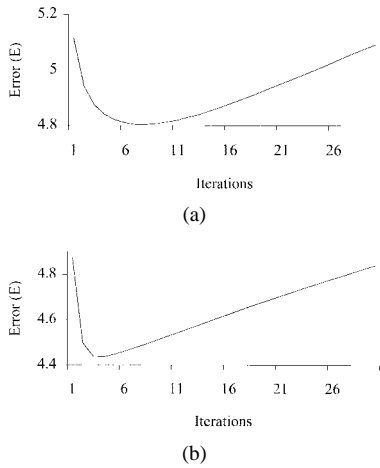


Fig. 11. Variation of the regulatory error metric (E) for noisy data (SNR = 10 dB): (a) Case 1 and (b) Case 2.

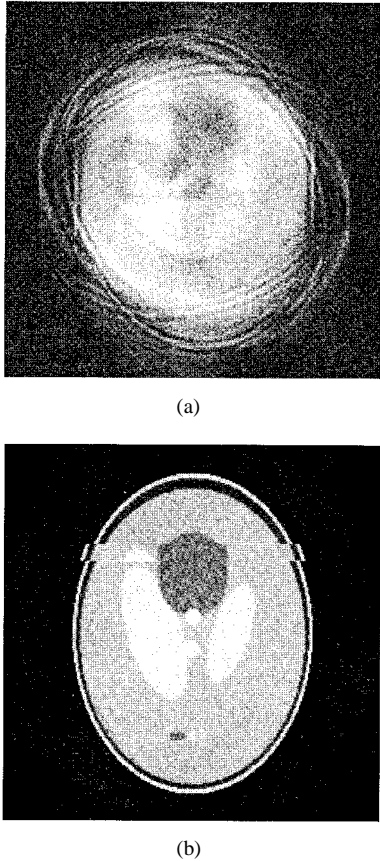


Fig. 12. (a) Artifacts image for Case 2 at SNR = 10 dB (MSE = 3180.528). (b) Reconstructed image using the proposed algorithm at SNR = 10 dB (MSE = 306.889).

instead of the expected solution. The number of elements in \mathcal{C}_o can be restricted by introducing additional *a priori* information in order to force the algorithm to converge toward the expected solution.

However, in practice, available *a priori* information is limited. Therefore, expectation of a unique solution is unrealistic. Hence, we have introduced the regulatory error metric, which indicates the closest possible reconstructed image to the expected result, at its minimum value. The iterations are terminated when E reaches its minimum.

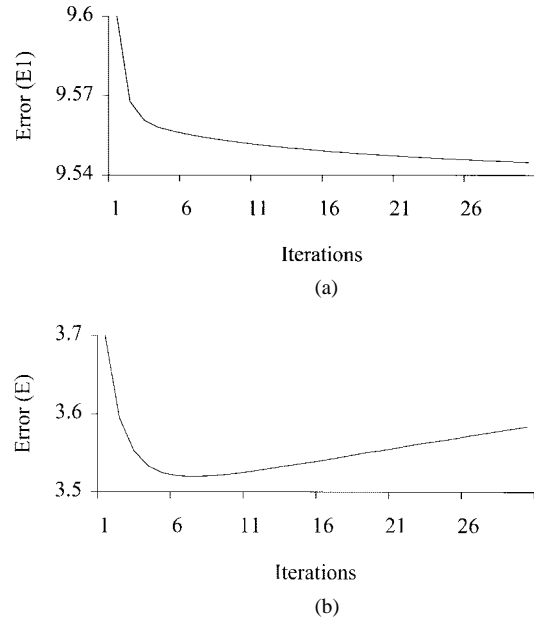


Fig. 13. Variation of E_1 and E for Case 3, with $\pm 1^\circ$ errors in motion parameter estimations: (a) E_1 and (b) E .

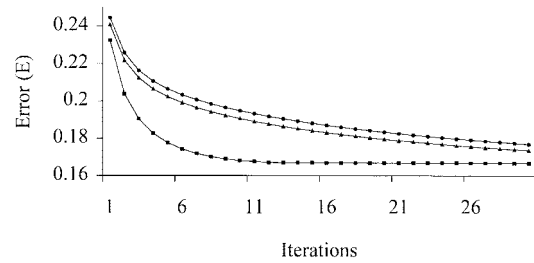


Fig. 14. Variation of E for Case 1, with 0% (—■—), 10% (—▲—), and 30% (—●—) increases in the area of the ROI.

In certain circumstances, the expected image may not belong to one or more convex sets. For example, the set \mathcal{C}_1 is violated when there is severe noise in the acquired data. \mathcal{C}_2 may be violated due to noise and interpolation errors. Therefore, proposed algorithm may not be able to converge to the original image. However, it can be shown that it is capable of improving the image quality compared to the bilinear superposition algorithm. In such a situation, E goes through a single minimum, although E_1 continue to decrease. The optimal image can be obtained by terminating the iterations at the minimum value of E .

Convergence properties of the algorithm was examined subjected to noisy data at 10-dB SNR. The results are shown in Figs. 10–12.

Data set in Case 3 was used to test the algorithm for continuous motion with $\pm 1^\circ$ errors in motion parameter estimations. Fig. 13 shows the results obtained. It can be observed that E_1 and E exhibit similar type of behavior as with noisy data. Errors in parameter estimations forces convex set \mathcal{C}_2 to be violated and, hence, the original object no longer is contained within \mathcal{C}_2 . However, the algorithm converges toward the solution for a finite number of iterations. The algorithm is terminated when E reaches its minimum.

The sensitivity to the accuracy of the selected ROI was investigated using 10% and 30% increases in the area of the ROI. The data set in Case 1 was used. The variation of E with the iterations is shown in Fig. 14. It can be observed that with larger estimates for the area of ROI, the initial convergence rate significantly decreases.

Each iteration of the algorithm takes less than 8 s to complete, on a Sun SPARC 2 station. Since the interpolation takes up bulk of the computational time, the additional computational time required to obtain approximately 80% improvement in MSE, is at most 25%, compared to the previous work [1].

VI. CONCLUSION

In this paper, an improved algorithm for suppression of in plane rotational motion artifacts in 2-D FT MR images has been presented. The major differences between this algorithm and other previous work [1], [2] are, optimal management of redundant data, using a weighted averaging scheme and iterative estimation of data in unfilled regions of the k -space, using POCS. The simulation results indicate that the algorithm effectively improve the quality of the final image. The iterative algorithm is also shown to be robust against noisy data and small errors in rotation angles. This algorithm is particularly suited for artifact correction of MR signals subjected to large angle rotations.

REFERENCES

- [1] R. A. Zoroofi, Y. Sato, S. Tamura, and H. Naito, "MRI artifact cancellation due to rigid motion in the imaging plane," *IEEE Trans. Med. Imag.*, vol. 15, pp. 768–784, Dec. 1996.
- [2] M. L. Wood, M. J. Shivji, and P. L. Stanchev, "Planer motion correction with use of k -space data acquired in Fourier MR imaging," *J. Magn. Reson. Imag.*, vol. 5, no. 1, pp. 57–64, 1995.
- [3] Y. H. Tseng, J. N. Hwang, and C. Yuan, "Motion artifact correction of MRI via iterative inverse problem solving," in *Proc. IEEE Image Processing Conf. '94*, pp. 871–875.
- [4] H. W. Korin, J. P. Felmlee, S. J. Riederer, and R. L. Ehman, "Spatial-frequency-tuned markers and adaptive correction for rotational motion," *Magn. Reson. Med.*, vol. 33, pp. 663–669, 1995.
- [5] M. L. Lauzon and B. K. Rutt, "Generalized k -space analysis and correction of motion effects in MR imaging," *Magn. Reson. Med.*, vol. 30, pp. 438–446, 1993.
- [6] M. Hedley, H. Yan, and D. Rosenfeld, "A modified Gerchberg–Saxton algorithm for one-dimensional motion artifact correction in MRI," *IEEE Trans. Signal Processing*, vol. 39, no. 6, pp. 1428–1433, 1991.
- [7] H. Yan and J. C. Gore, "An efficient algorithm for MR image reconstruction without low spatial frequencies," *IEEE Trans. Med. Imag.*, vol. 9, pp. 184–189, Apr. 1990.
- [8] H. Na, J. Shen, "A Fourier domain technique for ionospheric tomography," *Radio Sci.*, vol. 30, no. 3, pp. 747–754, 1995.
- [9] P. Feng, S. F. Yau, and Y. Bresler, "A multicoeset sampling approach to the missing cone problem in computer-aided tomography," in *Proc. 1996 IEEE ISCAS*, vol. 2, 1996, pp. 734–737.
- [10] K. K. R. Yu and S. F. Yau, "Solution of the missing cone problem by artificial neural network," in *Proc. 1994 IEEE ISCAS*, vol. 6, 1994, pp. 467–470.
- [11] M. I. Sezan and H. Stark, "Tomographic image reconstruction from incomplete view data by convex projections and direct Fourier inversion," *IEEE Trans. Med. Imag.*, vol. MI-3, pp. 91–98, Apr. 1984.
- [12] R. M. Glaeser, L. Tong, and S. H. Kim, "Three-dimensional reconstructions from incomplete data: Interpretability of density maps at 'atomic' resolution," *Ultramicroscopy*, vol. 27, no. 3, pp. 307–318, 1989.
- [13] D. C. Youla and H. Webb, "Image restoration by the method of convex projections: Pt. 1—Theory," *IEEE Trans. Med. Imag.*, vol. MI-1, pp. 81–94, Apr. 1982.
- [14] J. K. Riek, A. M. Tekalp, W. E. Smith, and E. Kwok, "Out-of-plane motion compensation in multislice spin-echo MRI," *IEEE Trans. Med. Imag.*, vol. 14, pp. 464–470, June 1995.
- [15] L. A. Shepp and B. F. Logan, "Reconstructing interior head tissue from X-ray transmissions," *IEEE Trans. Nucl. Sci.*, vol. NS-21, pp. 228–238, Jan. 1974.